Applying and validating Coulomb rate-and-state seismicity models in acoustic emission experiments

Heimisson, Elías Rafn; Naderloo, Milad; Chandra, Debanjan; Barnhoorn, Auke

DOI
10.1016/j.tecto.2024.230574

Publication date
2024

Document Version
Final published version

Published in
Tectonophysics

Citation (APA)
Heimisson, E. R., Naderloo, M., Chandra, D., & Barnhoorn, A. (2024). Applying and validating Coulomb rate-and-state seismicity models in acoustic emission experiments. *Tectonophysics*, *895*, Article 230574. https://doi.org/10.1016/j.tecto.2024.230574

Tectonophysics 895 (2025) 230574

Contents lists available at ScienceDirect

Tectonophysics

journal homepage: www.elsevier.com/locate/tecto

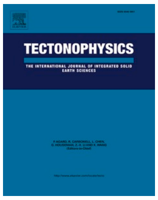

Applying and validating Coulomb rate-and-state seismicity models in acoustic emission experiments

Elías Rafn Heimisson [a,b,*], Milad Naderloo [c], Debanjan Chandra [c], Auke Barnhoorn [c]

[a] Institute of Earth Sciences, University of Iceland, Reykjavík, Iceland
[b] Swiss Seismological Service, ETH Zurich, Zurich, Switzerland
[c] Department of Geoscience and Engineering, Faculty of Civil Engineering and Geosciences, Delft University of Technology, Delft, the Netherlands

ARTICLE INFO

Keywords:
Coulomb rate-and-state
Fault mechanics
Seismicity
Triggered earthquakes
Acoustic emissions

ABSTRACT

A central goal of laboratory seismology is to infer large-scale seismic processes from small-scale experiments, with acoustic emissions (AE) being a common observable. These signals, indicative of microfracturing, slip localization, and damage evolution, are often paralleled with earthquakes to understand seismic behaviors. This study challenges traditional perspectives by applying Coulomb rate-and-state seismicity theory, originally developed for earthquake clustering, to AE experiments. This theory maps stressing history to seismicity rates using rate-and-state friction, however, its validity under controlled experimental conditions remains an open question. We conducted four experiments on a sawcut sample of red felser sandstone, representing a fault under variable stress conditions. Adjustments in loading rates and initial conditions revealed that, while a single free parameter A—related to the direct effect—should suffice, a rescaling of the model by 1.5 to 2.2 was necessary for fitting the data. Differences in values across experiments appeared mostly non-systematic, and partial data usage did not yield consistently systematic parameter migrations. These findings suggest that fault microstructure may complexly alter parameter values during loading beyond what is accounted for in the Coulomb rate-and-state theory. Nonetheless, with the introduction of the scaling parameter, the Coulomb rate-and-state theory effectively captures the fundamental aspects of AE responses to complex controlled loading histories.

1. Introduction

A significant challenge in earthquake seismology, as well as in many other fields, is that the subjects of interest—earthquakes and fault movements—cannot be studied in a controlled laboratory setting. The field largely depends on field observations of events where seismometers and other instruments are already in place, or increasingly, on numerical models. While both methods are extremely useful for testing theories and hypotheses, they are limited by considerable uncertainties about the true natural structures, heterogeneity, initial conditions, and especially the true state of stress in the crust.

However, controlled experiments are a rich and integral part of the seismological community's dialogue and discourse. These experiments are typically conducted on a centimeter scale, involving the compression of rocks with and without deviatoric stress through strain or stress controlled experiments. The samples can be sawcut, blocks, prefractured, powdered, or intact, and may have fluids injected or included under pressurized conditions. Temperature may also be controlled or varied. While such experiments have illuminated various aspects of earthquake and fault phenomena—for example, through acoustic emission (AE) experiments (e.g., Lockner, 1993; Lei and Ma, 2014; Naderloo et al., 2023b), and the derivation of frictional constitutive laws (e.g., Byerlee, 1978; Dieterich, 1972, 1979)—their interpretation is often limited by the fundamental question of scalability: Are the results applicable to natural faults? Some experiments have been carried out on a meter scale in traditional laboratory settings (e.g., Dieterich, 1981; Ke et al., 2018; Cebry et al., 2022), and more recently, experiments have been conducted directly on natural faults in mines (e.g., Guglielmi et al., 2015, 2021). The latter offers a compromise between measuring more observables under controlled conditions and capturing phenomena on actual, natural faults. However, even in these settings, knowledge of fault geometry, absolute stresses, and other critical parameters remains incomplete.

Thus, much of laboratory seismology involves extrapolating centimeter-scale results to natural fault scales. This extrapolation is well-founded on observations that demonstrate similar properties in both

---

* Corresponding author at: Institute of Earth Sciences, University of Iceland, Reykjavík, Iceland.
E-mail address: eliasrafn@hi.is (E.R. Heimisson).

https://doi.org/10.1016/j.tecto.2024.230574
Received 13 July 2024; Received in revised form 11 November 2024; Accepted 25 November 2024

scales. For instance, phenomena such as the Gutenberg-Richter law (Carpinteri et al., 2006), Omori's law of aftershocks (Vilhelm et al., 2017), and the Kaiser effect (Lavrov, 2003) manifest in both earthquakes occurring on kilometer-scale faults and in centimeter-scale laboratory experiments. Notably, the Kaiser effect was first identified in rock mechanics experiments before being recognized in seismic activity (Simpson et al., 1988; Heimisson et al., 2015). This underscores a long-standing tradition of utilizing small-scale experiments to understand natural earthquake and fault phenomena.

The theory proposed by Dieterich (1994) provided a physics-based model that links stressing history with seismicity production, forming the basis of what are often called Coulomb rate-and-state (CRS) models. In fact, CRS models deviate from the original theory of Dieterich (1994) only by a simple approximation, generally valid when the change in normal stress is minor compared to the initial normal stress (Heimisson and Segall, 2018). CRS models have been widely applied, for example, in studies of aftershocks (e.g., Harris and Simpson, 1998; Cattania et al., 2015), induced seismicity (e.g., Norbeck and Rubinstein, 2018; Zhai et al., 2019; Candela et al., 2019), and volcano tectonic earthquakes (e.g., Green et al., 2015; Heimisson and Segall, 2020). The foundational concept of CRS models, rate-and-state friction, is an empirical theory derived from rock friction experiments (Dieterich, 1979; Ruina, 1983; Marone, 1998). Consequently, CRS models also fall into the theme of applying small-scale laboratory results to large-scale earthquake processes. However, there are fundamental differences from the previously mentioned examples. Firstly, rate-and-state friction is based not on acoustic emission (AE) observations but on measuring the evolution of frictional resistance during controlled sliding between block interfaces. Secondly, the derivation and applications of the theory have been, to the best of our knowledge, exclusively used for studying earthquakes and the clustering of seismic activity rather than AE.

Here, we shift this perspective to explore whether the theory can be applied to the production of acoustic emissions (AE). In our controlled experiments, we test the theory under known stress conditions. We introduce a smooth sawcut into a sandstone sample to simulate a natural fault. By combining a constant stressing rate with rapid loading and unloading, we test various aspects of the theory, such as the manifestation of the Kaiser effect. Additionally, we vary the overall rate of loading and initially deviate from the assumption of a constant stressing rate to assess the model's applicability in low stressing rate regimes.

2. Methods and rationale

In this work, we carry out four experiments that aim to test the application of the CRS models to AE. The experiments differ only by their loading history. Initially, there are two experiments that adhere to the assumption of the Dieterich (1994) theory that the population of seismic sources is initially producing a fixed rate of events r at a stressing rate $\dot{\tau}_r$. We refer to these as the Dieterich, 1994 test (Fig. 1), and we carry out two variations where $\dot{\tau}_r$ varies by a factor of two, referred to as DS and DF (Dieterich Slow and Dieterich Fast, respectively). The other set of experiments violates the assumption of constant r at a stressing rate $\dot{\tau}_r$ at the time of the perturbation. We do this to test if the model can still be applied directly when the stressing rate has ceased for some time. This mimics applications of the CRS models in many induced seismicity settings, where there is little tectonic stressing rate and little background rate of seismicity at the time of perturbation, such as was the case in the Groningen gas field in the Netherlands. We can thus explore if there is a development of a stress threshold as postulated by Heimisson et al. (2021). We refer to this as the threshold test (Fig. 1) and these experiments as TS and TF (Threshold Slow and Threshold Fast, respectively).

There are four different phases of loading (Fig. 1), each designed to test various predictions and assumptions of the theory. Phase I assesses whether there is a constant rate of AE under a constant stressing rate. This phase is not intended for direct modeling as it serves to establish the appropriate initial conditions for the CRS model. Phase II differs between the D and T experiments; in the D experiments, it tests the Kaiser effect by creating rapid oscillations in loading and unloading (at approximately $10\dot{\tau}_r$). In the T experiments, Phase II includes an initial part where loading is halted before the oscillating stresses. In both scenarios, modeling of the AE response begins at the onset of the oscillating stress part also known as the Kaiser effect test. Phase III involves reloading beyond the previous maximum stress at the original background rate $\dot{\tau}_r$, which, if the CRS model is applicable, should result in the reemergence of r. Phase IV tests the sample with a rapid step load (conducted at approximately $10\dot{\tau}_r$) and continues monitoring the AE without further loading, as discussed further in Section 3. The loading is controlled by strain, but the measured stress state is used as an input. Due to the nature of strain loading, the planned loading curves depicted in Fig. 1 cannot be replicated exactly.

From these loading procedures, we derive the shear and normal stressing histories on the fault plane of the sample. This allows us to reduce the number of free parameters to one or two, depending on the assumptions made, and to carry out fitting of the observed AE rate. More

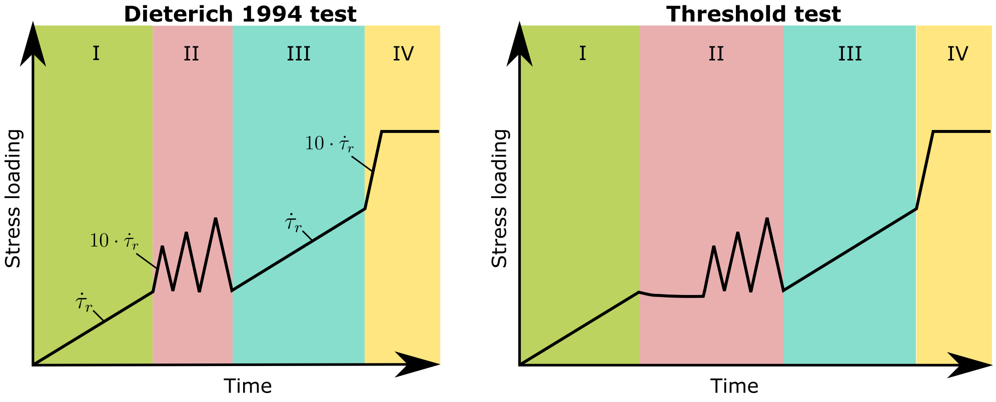

Fig. 1. Two loading strategies are illustrated. On the left, to test the response of the sample based on the assumptions regarding initial conditions of the Dieterich (1994) theory, loading is divided into four phases: Phase I applies a constant stressing rate until AE is observed at a constant rate; Phase II introduces three oscillations to activate the Kaiser effect; Phase III involves reloading at a constant rate; and Phase IV concludes with a stress step and halt in loading. On the right panel, a halt in loading is introduced before oscillatory stresses to explore the sensitivity to violating the initial conditions assumptions and the possible development of a threshold.

details are discussed in the following section.

3. Experimental procedure

The experimental setup closely follows that described by Naderloo et al. (2023a), but is reviewed here for completeness.

3.1. Preparation of samples

For this series of experiments, Red Felser sandstone from the Rotliegend formation near Kaiserslautern, Germany, was selected for its uniformity and capacity to sustain significant loading without undergoing complete failure. Each specimen was drilled from the same rock slab to ensure uniformity, with a diameter of 30 mm and a length of approximately 70 mm. The samples exhibited an average density of 2.1 ± 0.015 g/cm^3 and a porosity of 21.14 ± 0.7 % (see Naderloo et al., 2023a). To simulate a fault plane, cylindrical samples measuring 75 mm in length and 30 mm in diameter were cut at a 30° angle to the cylinder's vertical axis (Fig. 2). The saw-cut surfaces were carefully cleaned to remove any loose rock particles and grains. The smooth and clean cut surface, as well as the significant uniformity of the rock allow us to accurately estimate the stress on cut surface from the confining stresses.

3.2. Testing apparatus

For the triaxial fault reactivation experiments, we utilized an instrumented Hoek cell capable of withstanding a maximum confining pressure of 70 MPa. This cell was mounted on a uniaxial servo-control loading machine with maximum capacity of 500kN, which provided a resolution of ±0.05 kN, responsible for applying the axial stress (σ_1) (see Fig. 2). To protect the rock sample from the confining oil, we employed a specialized silicon jacket. Embedded within this jacket were eight piezoelectric transducers, each 5 mm in diameter and 1 mm thick. These transducers were in direct contact with the rock surface, enabling them to capture microseismic events or acoustic emissions (AE). The signals from these transducers were amplified using pre-amplifiers to enhance data acquisition, which was then processed through the Richter continuous data acquisition system. Vertical deformations of the samples were measured by two Linear Variable Displacement Transformers (LVDTs) able to measure displacement up to 2 mm with a maximum resolution of 0.1 μm. The LVDTs are placed on either side of the bottom platten of the Hoek cell and the strain in the tested specimen is calculated based on the average displacement of both LVDTs.

We used a Richter acoustic emission system for capturing and detecting microseismic activities across various stress patterns and rates, as depicted in Fig. 2. The Richter system features a versatile, multichannel data acquisition setup with 16-bit ADC resolution, enabling simultaneous and synchronous sampling across all input channels. Continuous waveforms were recorded at a sampling rate of 2 MHz and an input impedance of 50 Ohms, using the ExStream software. While ExStream handled the recording of acoustic emission data, the raw waveform data were processed and managed using the Insite Seismic Processor software. This involved converting continuous waveform data into individual events based on predefined trigger logic. An event was recorded when five or more transducers exceeded a voltage threshold of approximately 25 mV within a 480-microsecond window at 2 MHz sampling rate. The amplitude threshold was set at 1 mV, a level carefully chosen to mitigate the effects of various background noises typical in the laboratory environment.

3.3. Loading protocol

At the beginning of Section 2, we discussed the general concepts behind the loading protocol. Here, we provide a detailed review of the specifics. Notably, we employ displacement loading rather than stress loading; this is to avoid driving the sawcut to an uncontrollable throughgoing failure at the higher stress levels. Nevertheless, we effectively achieve stress loading as depicted in Fig. 1 by adjusting the two loading rates and monitoring the measured stress state. The load cell and LVDTs provide nearly instantaneous feedback, ensuring that any changes in stress due to piston movement are immediately reflected in the recorded data, the uncertainty of the measured stresses is around the third decimal point. Towards the end of the loading protocol, deviations from a linear strain-stress relationship are observed, leading to differences between the observed stress loading (Fig. 3) and what is illustrated.

In all experiments, we initially isotropically load the sample to establish a net hydrostatic compressive state of 20 MPa with $\sigma_1 = \sigma_3$ (Fig. 3). Deviatoric stress is then induced by moving the axial loading piston while keeping σ_3 constant (Fig. 2). The piston is moved at either 0.0001 mm/s and 0.001 mm/s (representing $\dot{\tau}_r$ and $10\dot{\tau}_r$ in Fig. 1

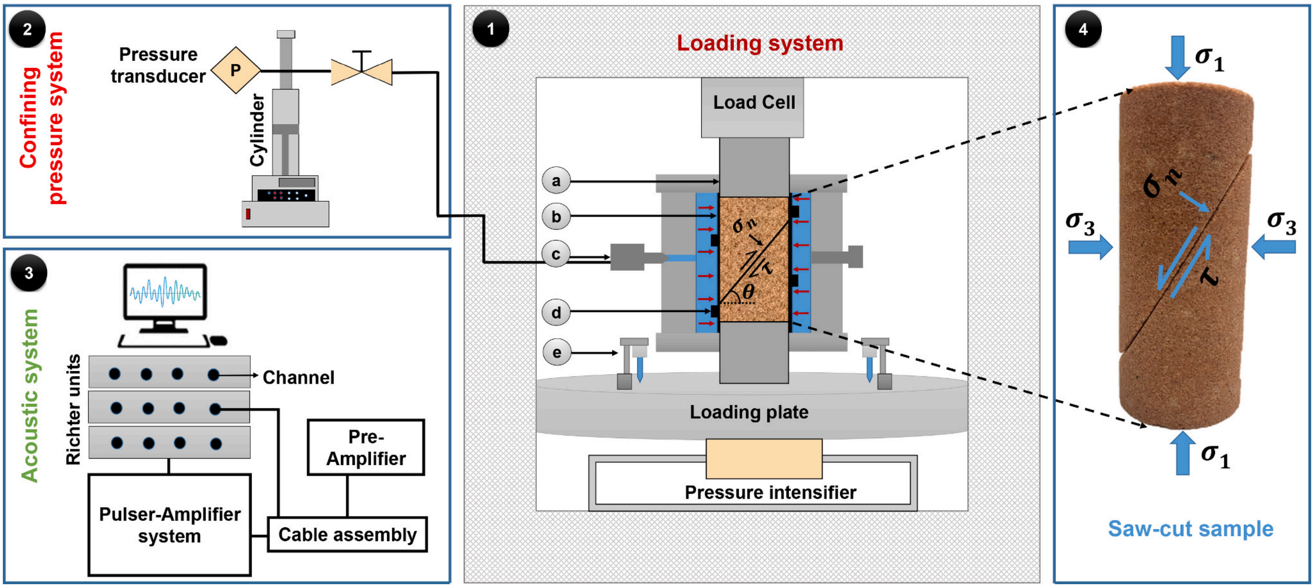

Fig. 2. Schematic of the experimental setup, illustrating the different units involved: 1) Loading system, which includes (a) the loading piston, (b) silicon jacket, (c) confining oil inlet, (d) eight acoustic emission sensor, (e) two Linear Variable Differential Transformer (LVDT) for measuring axial deformation; 2) Confining pressure system; 3) Acoustic system; and 4) saw-cut sample.

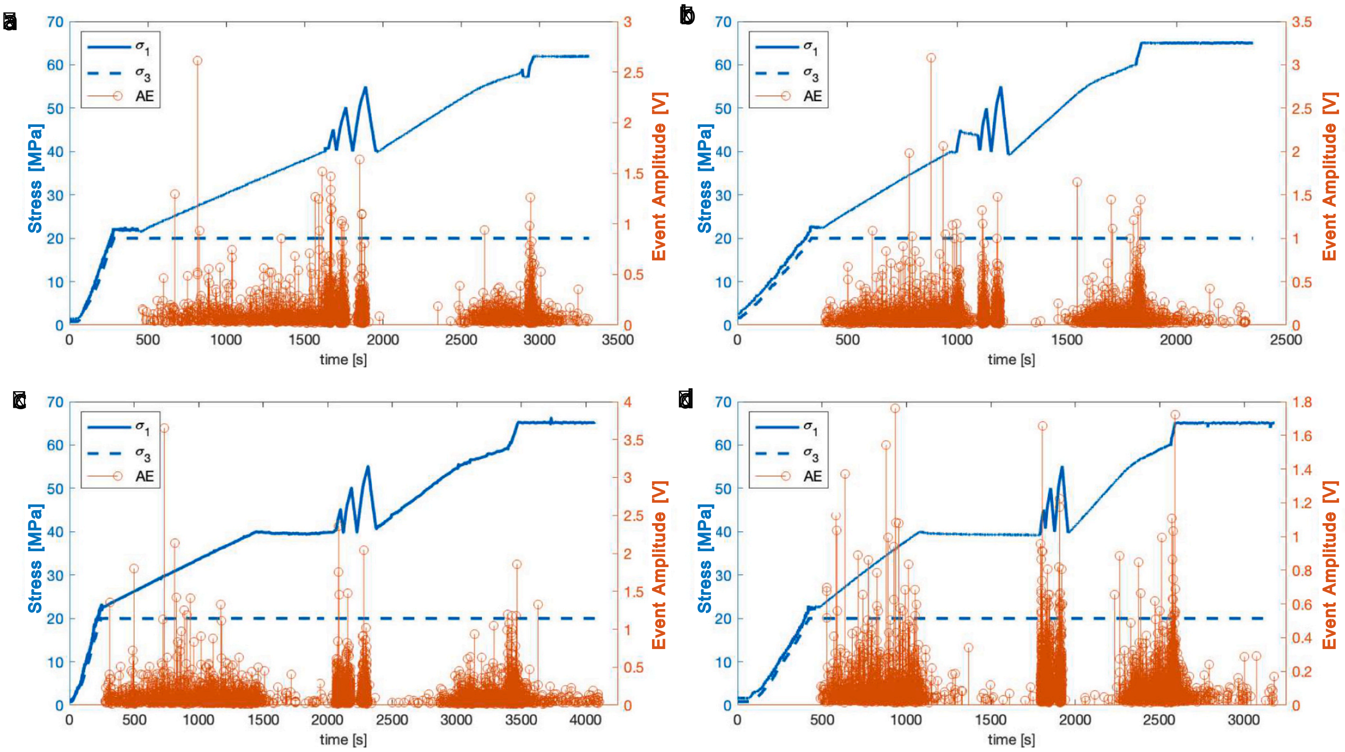

Fig. 3. Overview of the observed data from each experiment, where σ_1 and σ_3 are directly measured as a result of displacement loading, and acoustic emissions (AE) are detected simultaneously. Panel a represents the DS experiment, panel b shows the DF experiment, panel c depicts the TS experiment, and panel d illustrates the TF experiment. The manifestation of the Kaiser effect is clearly identifiable in the data.

respectively) for the S (slow) experiments, and at 0.0002 mm/s and 0.002 mm/s for the F (fast) experiments. In the T (threshold) experiments, where no loading is applied, the axial piston was halted. Phase I is carried out until σ_1 reaches 40 MPa (see Fig. 1 for reference). The oscillatory part of Phase II consists of 3 sawtooth peaks, each incrementing by 5 MPa. In Phase III, we reach $\sigma_1 = 60$ MPa, and Phase IV involves an increase to $\sigma_1 = 65$ MPa, followed by a hold where the axial piston remains static. It is during the latter part of Phase III and throughout Phase IV that deviations from linearity become significant and deviations from the idealized protocol are more pronounced.

4. Theory

Using a spring-slider analysis, one can derive a relationship for the seismicity rate R of a distribution of seismic sources that fail at a fixed rate r under a background shear stressing rate $\dot{\tau}_r$ (Heimisson and Segall, 2018).

$$\frac{R}{r} = \frac{K(t)}{1 + \frac{1}{t_a}\int_0^t K(t')dt'}, \tag{1}$$

where $t_a = A\sigma_0/\dot{\tau}_r$ is the characteristic decay time of aftershocks (Dieterich, 1994). Here, A represents a constitutive parameter that scales the rate dependence of friction and is associated with the direct effect, while σ_0 is the initial effective normal stress at the time the system is perturbed, where compression is defined positive. The function $K(t)$ is defined as

$$K(t) = exp\left(\frac{\tau(t)}{A\sigma(t)} - \frac{\tau_0}{A\sigma_0}\right)\left(\frac{\sigma(t)}{\sigma_0}\right)^{\alpha/A}, \tag{2}$$

where τ_0 is the initial shear stress, akin to σ_0. Therefore, $\tau(t)$ and $\sigma(t)$ represent the initial stress plus any time-dependent perturbation, i.e., $\tau(t) = \tau_0 + \Delta\tau(t)$ and $\sigma(t) = \sigma_0 + \Delta\sigma(t)$. The parameter α is the Linker-Dieterich constant (Linker and Dieterich, 1992), which relates state changes to normal stress variations.

While $K(t)$ described above is more theoretically accurate, practitioners typically use an approximation based on Coulomb stress. This approximation is valid for relatively small perturbations in $\sigma(t)$ compared to σ_0 (Heimisson and Segall, 2018), and under this condition, the theories derived by Dieterich (1994) and Heimisson and Segall (2018) converge. Given the prevalent use of this formulation, we will focus on it in this paper but will briefly discuss the results in terms of the more theoretically accurate form as well. Under the Coulomb stress approximation, Eq. (1) can be rewritten as:

$$\frac{R}{r} = \frac{exp(S(t'))}{1 + \frac{1}{t_a}\int_0^t exp(S(t'))dt'}, \tag{3}$$

where $S(t) = \Delta\tau(t) - \mu\Delta\sigma(t)$ represents a modified Coulomb stress with $\mu = \tau_0/\sigma_0 - \alpha$. Additionally, in $t_a = A\sigma_0/\dot{\tau}_r$, we modify the background stressing rate as $\dot{\tau}_r = \dot{\tau}(t) - \mu\dot{\sigma}_r(t)$. Generally, solving Eq. (3) directly is quite effective. However, as depicted in Fig. 4, the stress changes in our experiments are significantly larger—ranging from several to ten MPa—compared to those in typical triggering studies (Hainzl et al., 2010), which are often an order of magnitude smaller. This difference raises computational challenges, as the exponential function can become too large to handle effectively, even though the value of R may still be reasonable. This is a common problem in numerical computations and various methods exist to address it. In our case, we have opted to formulate the equation as an ordinary differential equation (ODE) (see Heimisson, 2019).

$$\frac{R}{r} = exp\left(\frac{S(t') - \dot{\tau}_r N/r}{A\sigma_0}\right), \tag{4}$$

where N represents the cumulative number of events, and $dN/dt = R$. This equation can be integrated using standard ODE solving methods. The formulation is more stable for handling very large stress changes

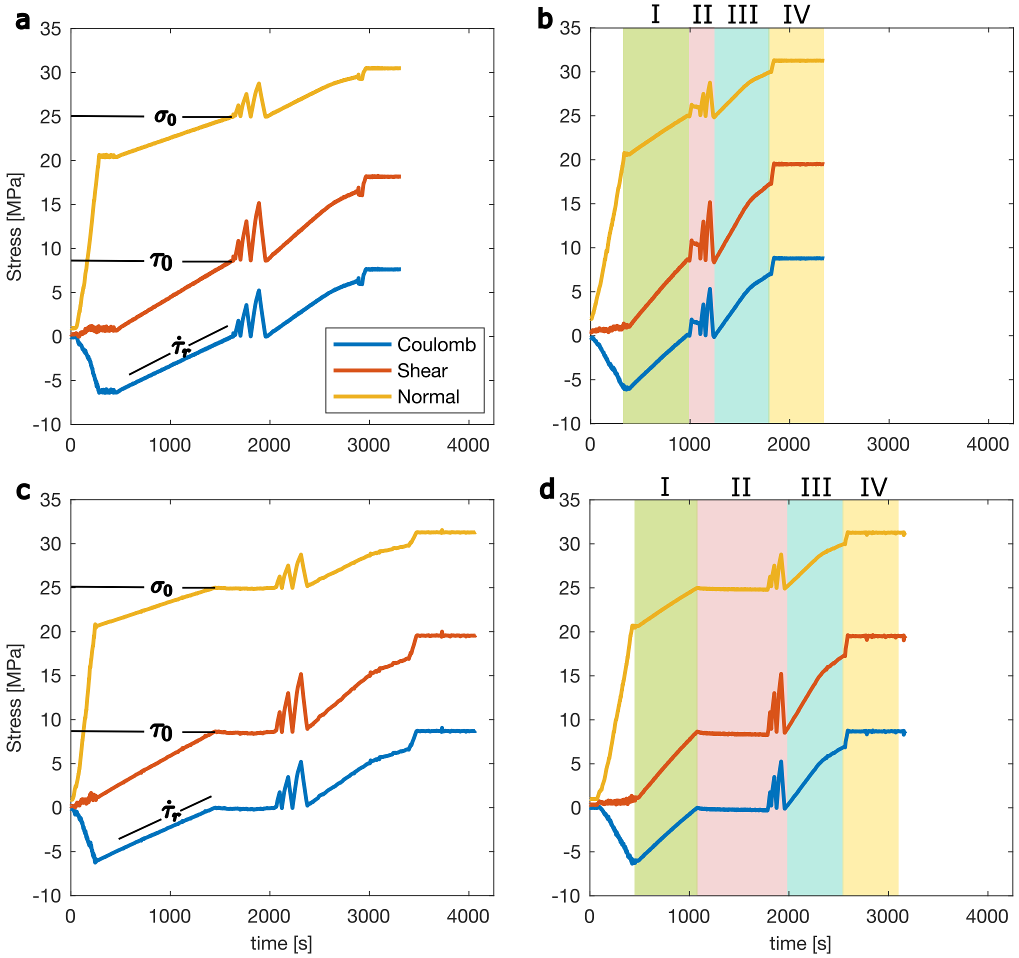

Fig. 4. Calculated normal, shear, and modified Coulomb stresses on the cut fault, along with the Coulomb stressing rate, and initial shear and normal stress calculations for both D and F experiments. Panel a represents the DS experiment, panel b depicts the DF experiment, panel c shows the TS experiment, and panel d illustrates the TF experiment. Panels b and d show the experimental phases for both D and F experiments. The initial decrease in Coulomb stress, prior to Phase I, corresponds to the initial 20 MPa confinement of the sample. This step strengthens the interface and the surrounding rock, producing no detectable AE events (see Fig. 3). As such, it is not considered part of the loading protocol.

because the argument of the exponential function remains within a reasonable range, even though $S(t)$ may be significantly large. This stability arises because N grows and effectively subtracts from the exponential argument, mitigating the impact of large values of $S(t)$.

4.1. Modeling and fitting procedure

Using the detected AE data (Fig. 3), we filtered the catalog to ensure completeness, which was estimated at a threshold of 0.1 V in all cases (see supplementary figs. S1-S4). We further tested estimating the parameters with a more stringent threshold of 0.2 V and found good agreement. The comparison between the theoretical model (Eq. (4)) and observed data was quantified using a time-dependent Poissonian loglikelihood function (e.g., Daley et al., 2003):

$$logL = \sum_{i=1}^{N} log(R(t_i)) - \int_{t_s}^{t_f} R(t')dt', \tag{5}$$

where t_i are the observed event times occurring between t_s and t_f. Here, t_s is defined as the onset of saw-tooth loading in Phase II, and t_f is defined as either the time of the last observed event or the point when measurements of the stress state conclude. We also explore systematically varying t_f in our analysis. Eq. (5) allows for error analysis via bootstrapping by resampling t_i with replacement. During resampling, we account for a possible 1-s error in synchronizing event observations with stress measurements, which are plotted together in Fig. 3. This error analysis method will be demonstrated in the Results section.

Phase I of the loading (Fig. 1) essentially allows us to constrain all parameters mentioned above except A and α. This initial loading phase helps us determine σ_0, τ_0, and $\dot{\tau}_r$, while simultaneously measuring $\boldsymbol{r}$. The selection of σ_0, τ_0, and $\dot{\tau}_r$ is depicted in Fig. 4 for both D and T experiments. The rate r is calculated in Phase I by computing the number of events above completeness in the last 500 s of this phase and dividing by 500 s. During this interval, the seismicity rate was observed to be steady.

During preliminary testing, it quickly became apparent that all inversions for all experiments forced α towards zero. It was later discovered that reducing the background stressing rate $\dot{\tau}_r$ improved the fit, as α, which must lie between 0 and τ_0/σ_0, can only increase the background stressing rate because $\dot{\sigma}_r$ is positive (indicating increased compression, as shown in Fig. 4). This condition implies that a value greater than 0 for α is never favored. Given this and the ongoing debate over the value of α and how the state dependence of normal stress should be interpreted or modeled (as discussed by sources like (Linker and Dieterich, 1992; Prakash, 1998; Kilgore et al., 2012)), we decided to set α to 0.

During the exploratory phase of data analysis and modeling, it became apparent that although the shape of the seismicity rate curves could be reasonably well matched by fitting only the parameter A, the absolute amplitude of these curves consistently fell short. Specifically, the best fit typically underpredicted the number of events by a factor of 1.5 to 2. This discrepancy might seem manageable at first glance, as a single parameter fit already captures a significant portion of the data's characteristics. In certain applications of the Coulomb rate-and-state theory, the emphasis is often placed more on replicating the shape rather than the absolute magnitude of the seismicity rate curves (e.g., Zhai et al., 2019).

Two strategies emerged as effective in achieving a quantitative match for both the amplitude and the shape of the curves. The first strategy involved adjusting the seismicity rate r, effectively scaling the entire curve. The second strategy entailed modifying the background stressing rate $\dot{\tau}_r$, either by changing the ratio τ_0/σ_0 or by introducing an unknown scaling factor. Given that the state of stress was directly measured, it seemed more prudent to consider r as an adjustable parameter. This approach generally yielded a better fit compared to modifying $\dot{\tau}_r$, and a similar fit when both were adjusted in conjunction with A. Furthermore, during phases III and IV, a deviation from linearity between strain loading and stress was observed, indicative of tertiary creep and damage evolution (as seen in Fig. 5a). This phenomenon could potentially alter the productivity of the interface or create new off-fault AE-producing locations.

Additionally, the original derivation of the theory presupposes that seismic sources are initially far from a steady state, a condition assumed valid if these are the sources triggered during the activity spanning t_a (Heimisson and Segall, 2018). In our experiments, we introduce significantly large stress changes and continue stressing well beyond the inferred t_a duration (10–40 s, as deduced from the model inversions in Fig. 5). Consequently, it's likely that we are violating the assumption that participating seismic sources are already above steady state and are accelerating towards instability. It, therefore, seems reasonable to hypothesize that r varies over time. In the subsequent results section, we compare this model-inferred r_{inv} against the initially measured r_{true}, while also considering adjustments to A.

5. Results

A primary focus of this study is to assess whether the acoustic emission (AE) data from slower and faster loading (S and F) experiments can be adequately fit using Coulomb rate-and-state theory, and to evaluate the model's performance under deviations from the Dieterich (1994) conditions, specifically the Threshold conditions (D and T). From Fig. 5, we observe that the model achieves a fairly reasonable fit using just two free parameters.

Fig. 5 displays a spread of solutions from bootstrapping, as explained

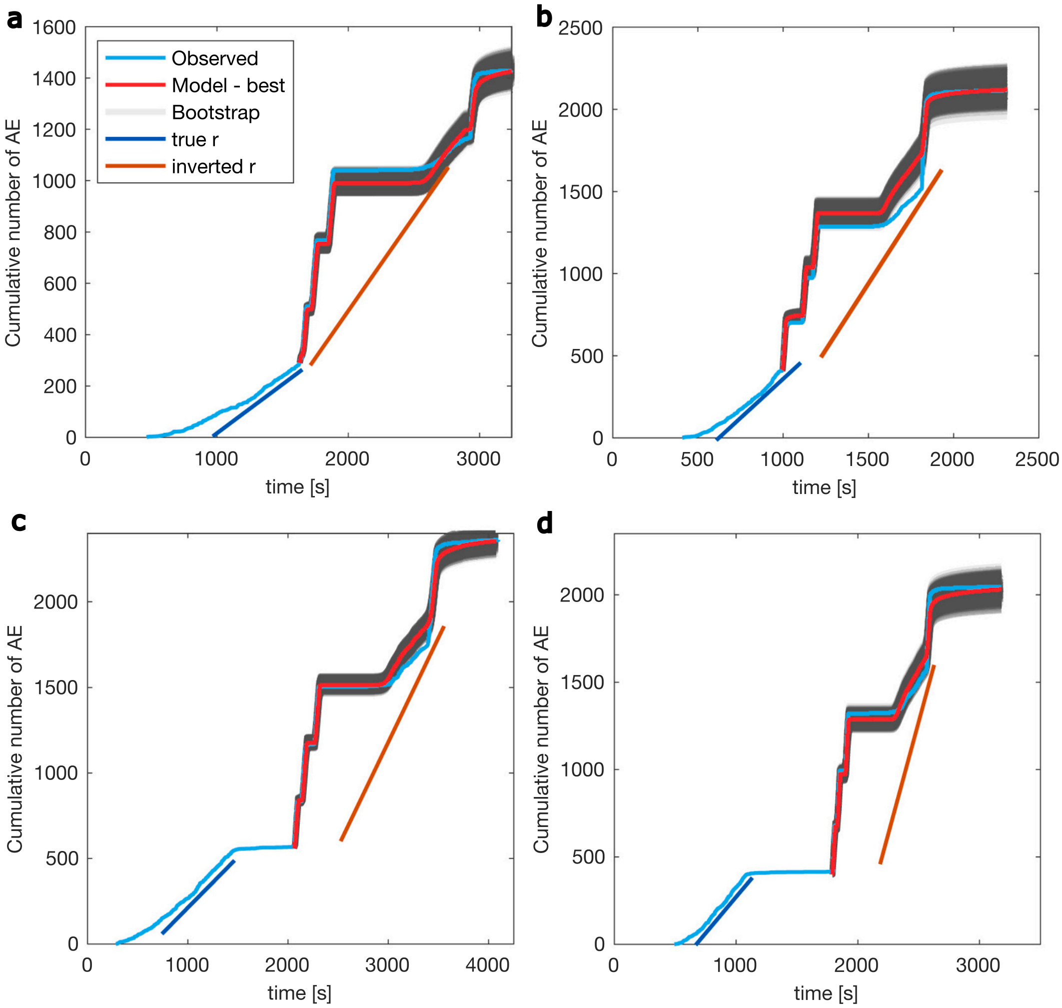

Fig. 5. Results from maximizing the loglikelihood function (Eq. (5)) for the entire dataset. The figure shows the observed cumulative number of events (after filtering for completeness) in light blue, the preferred model (fit to data without resampling) in red, and the dark grey zone represents overlapping model fits from bootstrapping, indicating the spread of the solution. Panel a is the DS experiment, b is the DF experiment, c is the TS experiment, and d is the TF experiment. The blue straight line indicates the slope of r_{true}, and the brown straight line represents the slope of r_{inv}. (For interpretation of the references to color in this figure legend, the reader is referred to the web version of this article.)

in Section 4.1. The red line represents the result where no resampling was conducted. Generally, the observed data falls within the range of the bootstrap results, except for certain segments in the DF and TS experiments (panels b and c), particularly where reloading exceeds the previous maximum stress state following the incremental saw-tooth loading. This is also the region where we observe signs of tertiary creep and nonlinearity between strain loading and stress due to significantly higher differential stress. Interestingly, the T experiments (panels c and d) show a similar level of agreement with the data despite there being no loading prior to the onset of the saw-tooth loading. Although no development of a stress threshold was observed under the experimental holds, the effects of a threshold induced by the Kaiser effect are well captured in both the experiments and the model.

Analysis of the parameter ranges is presented in Fig. 6a. Notably, three of the experiments can be uniformly fit with a single value of $A \approx 0.0065$, aligning well within the typical range of 0.004 to 0.012 cited by Dieterich (1994) for laboratory experiments under non-hydrothermal conditions. The consistent estimate of A, calculated through the Coulomb rate-and-state theory and compared with direct measurements from velocity stepping experiments, reinforces confidence in the theoretical framework. However, one experiment (DF) exhibits an A value slightly lower than the others. Fig. 6a also displays the ratio of the inverted r (from model fitting) to the measured (or true) r from Phase I. The ratios across the experiments range from 1.5 to 2.2, with some overlap but no apparent systematic trends. For instance, TS and DF show overlapping ranges, as do DS and TF, indicating that the most dissimilar experiments in terms of conditions exhibit the most similar r values. While not depicted here, it is important to note that σ_0 remains roughly consistent across all experiments. Additionally, S and F experiments differ in their $\dot{\tau}_r$ values by a factor of two. Consequently, when calculating $t_a = A\sigma_0/\dot{\tau}_r$, the duration is indeed about twice as long for S experiments compared to F, consistent with theoretical expectations.

As we systematically extend the time window—keeping t_s fixed but extending t_f—we observe migration in the model parameters. The value of A decreases, albeit slightly for DF (Fig. 6b), but more significantly for DS, to a point where there is little overlap between the bootstrapped distributions from the shorter and longer time windows. Despite these changes, it could be argued that the parameter remains fairly stable. Interestingly, r_{inv} initially decreases and then increases in both cases, with the smallest value occuring when t_f is in phase III in both cases. This behavior is unexpected since the values estimated from the shorter time windows do not align closely with r_{true}. Two simulations demonstrating this are shown in Fig. 7 for 500 s and 1250s (shaded color corresponds to the time window length and matches the colors in Fig. 6b). In Fig. 7, the fit appears excellent when only the initial part of the AE data is used, despite $r_{inv} \approx 2{\cdot}r_{true}$. Incorporating more data results in a fit that is not optimal for either the first or second half of the loading protocol. Notably, Phase III under the $\dot{\tau}_r$ shows a more or less steady seismicity rate approximating r_{true}. Indeed, in Phase III depicted in Fig. 5, the models tend to overpredict the steady seismicity rate because $r_{inv} > r_{true}$. However, using a higher r_{inv} compensates for other phases (II and III) where stresses increase rapidly and do not fit well with a lower r.

6. Discussion

6.1. Reconciling r_{inv} and r_{true}

One possible explanation for the discrepancy between r_{inv} and r_{true} is that r is influenced by the stress loading itself. The increased stressing rate during sawcut loading may make the interface more productive, thereby altering r. The fact that r_{true} reappears in Phase III, though less distinctly, suggests a potentially instantaneous link between r and the stressing rate. However, this effect is not pronounced, and the entire AE catalog can be reasonably fit with a single value that attempts to reconcile this variability. In Fig. 6, we observe that r_{inv} for the S (slow) and F (fast) protocols shows no apparent correlation, even though $\dot{\tau}_r$ is modified by a factor of 2. This indicates that if r is dependent on the stressing rate and the relationship is not straightforward, or it may not be discernible over a narrow range due to intrinsic differences in r resulting from varying microstructures on the cut fault. It may also be possible that r_{true} is underestimated and could be inferred by grain production and crushing, which are processes more likely in the early stages of loading and are physically different from the AE due to micro slip in the later stages.

An experiment that incrementally increases and maintains a constant stressing rate over a duration longer than t_a (approximately 10–40 s in this case) could potentially confirm or refute a more complex dependence of r on the instantaneous applied stress. It is noteworthy that we attempted to fit models using the more theoretically accurate Kernel function provided in Eq. (2). While variations in normal stress were sufficient to induce some changes in the parameter estimates, this formulation did not resolve the discrepancy between r_{inv} and r_{true} nor did it yield a significantly better fit.

6.2. Event locations

Accurate localization of AE events in this study was challenged by limitations in sensor configuration. Although we utilized eight sensors, the exposed nature of the sensors, lack of proper packing, and

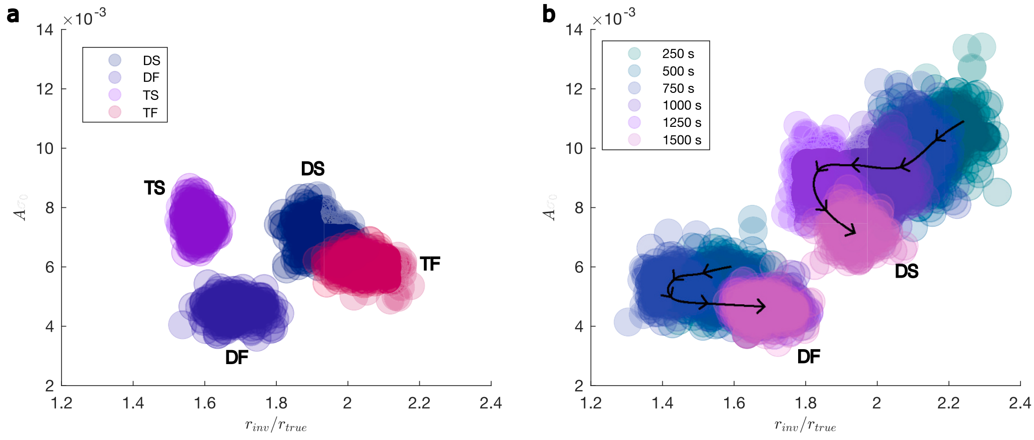

Fig. 6. Parameter ranges estimated from bootstrapping for (a) the entire dataset and (b) from systematically varying t_f in Eq. (5) for only the DS and DF experiments, thus incorporating progressively more data. Note labels for each dot color indicate $t_f - t_s$. For each time window, bootstrapping is conducted, and arrows indicate how the parameters migrated as a longer time window was used.

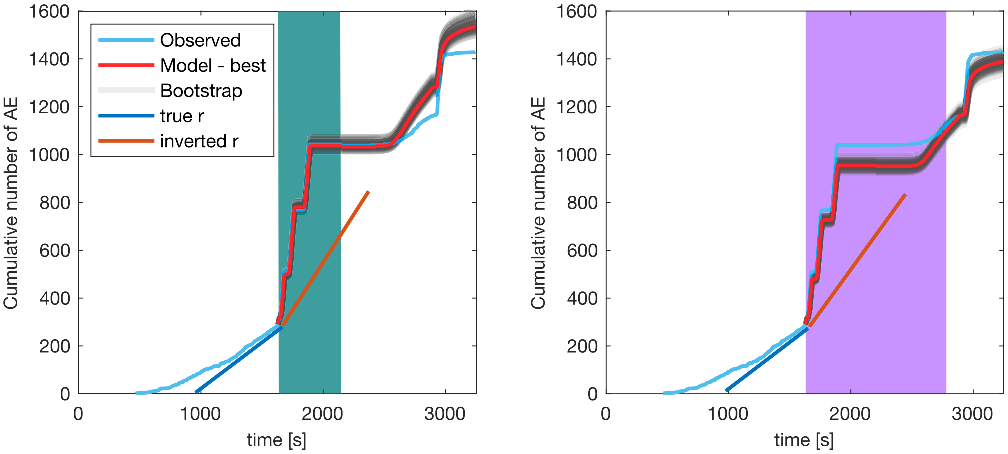

Fig. 7. Modeling of shorter time windows for DS experiments, following the same procedure as in Fig. 5a. Due to parameter estimates being less stable with shorter time windows, as demonstrated in Fig. 6, there is a more general mismatch than when using the entire dataset. However, the shorter time window yields an excellent initial fit, despite r_{inv} being significantly larger than r_{true}.

inadequate calibration resulted in suboptimal P- and S-wave arrival times, leading to uncertainty in pinpointing the exact locations of the events. Despite these limitations, the evidence strongly suggests that the majority of AE events originated from frictional sliding along the saw-cut fault plane, rather than from cracking of the intact rock mass.

AE activity was detected almost immediately upon the application of axial loading, with some events exhibiting relatively high amplitudes. According to Naderloo et al. (2023a), in intact Red Felsic rock under uniaxial loading without confinement, AE events typically begin to occur at around 30 MPa due to the onset of cracking. In our experiments, however, the rock was confined at 20 MPa, and confinement significantly increases the deviatoric stresses required to initiate cracking in the intact rock. Therefore, cracking of the intact rock would be expected to occur only at higher deviatoric stresses than those applied in our experimental setup. Furthermore, the absence of significant nonlinearity in the stress-strain profile, aside from some in Phase IV, indicates that the rock mass remained largely elastic and that plastic deformation, which would accompany significant cracking, did not occur.

Given these observations, it is most likely that the AE events are primarily associated with frictional sliding along the saw-cut fault plane. The rapid onset of AE activity, combined with the experimental conditions and the lack of stress-strain nonlinearity, supports this interpretation. While minor AE events may have been generated by inelastic deformation within the intact body of the rock, these would have been minimal in comparison to the dominant frictional processes occurring along the fault plane.

6.3. *Threshold after a strain hold*

A key motivation for this project was to determine if a stress threshold could develop if we ceased loading the sample after Phase I, before initiating the sawcut steps. This inquiry was inspired by observations of delayed seismicity onset in certain intra-plate settings, such as Groningen and Oklahoma (Zhai et al., 2019; Candela et al., 2019), and by a modified threshold Coulomb rate-and-state theory (Heimisson et al., 2021). This theory posits that a stress threshold must be overcome before the classical Dieterich (1994) formalism becomes applicable. Our analysis of the data revealed that no significant threshold developed; seismic activity commenced almost immediately with the onset of the first sawtooth cycle, within our ability to resolve AE activity and stresses. This outcome is not inconsistent with the theory of Heimisson et al. (2021), as a small or zero threshold value would effectively reduce it to the standard Coulomb rate-and-state theory. Furthermore, the threshold test conducted in Phase II was relatively brief and under a fairly low stress state. We hypothesize that if a threshold test were conducted over a longer period and at a higher stress level, a clearer threshold might emerge, but this remains to be verified in future studies. In some respects, this outcome is favorable for the standard Coulomb rate-and-state model, suggesting that it might be applicable even when the precondition of constant seismicity at the time of perturbation is not met.

6.4. *Wider applications*

Applying the Coulomb rate-and-state model to field-scale studies of triggered seismicity introduces substantial uncertainties, particularly regarding fault orientation and the values of τ_0 and σ_0. Stress changes in such studies need to be interpreted through models that may not account for all affecting processes. In contrast, our study benefits from significantly reduced uncertainty: we create a specific fault, directly measure stress, and control the stress field, thereby minimizing the impact of extraneous processes. However, extrapolating our results raises questions of scale and whether acoustic emissions (AE) can be considered as micro-earthquakes. Since AE may be caused by various processes, and only shearing related AE might be representative of earthquake, then our results suggest that the model could help distinguish between AE cause by shear movement and other causes.

Assuming AEs can be analogized to earthquakes, our findings offer several insights. In field-scale applications, the parameter $A\sigma_0$ is typically inverted from aftershock data, often yielding values between 0.01 and 0.1 MPa (Hainzl et al., 2010). If A is within the typical laboratory value range of 0.004 to 0.012, this suggests that the effective normal stress is significantly lower than what might be predicted by a simple lithostatic minus hydrostatic pressure model, a discrepancy that has led some to favor afterslip-driven aftershock theories (Perfettini et al., 2018). In our experiments, known σ_0 values yielded $A\sigma_0$ between 0.1 and 0.2 MPa, and A values between about 0.004 and 0.009—aligning with the upper range inferred in field studies but typical for laboratory studies, albeit at the lower end. This supports the hypothesis that σ_0 may be lower than expected, potentially due to elevated pore pressures at depth.

Our experiments also explored significant stress perturbations of around 10 MPa, compared to most field studies of triggering which consider stress transfers of less than 1 MPa (King et al., 1994). This suggests that the model can be applied to high-stress environments, such as near boreholes during fracking injections, though discrepancies between r_{inv} and r_{true} may be more likely to emerge in these cases.

Furthermore, Coulomb rate-and-state models have broad applications beyond studying earthquake triggering. They could be valuable in AE monitoring and characterization, which are crucial for assessing structural health and for material testing and design, for example for subsurface geothermal or CO2/H2 storage operations. For instance, these models could predict AE production at higher stress levels, even if catastrophic failure is not the intention. Moreover, in simulations of structures, the models could help identify which configurations produce more AEs under specific conditions. It is important to note that in material testing and many field applications, fault cuts are not predefined, complicating the calculation of Coulomb stresses. However, using the maximum Coulomb stress, which is independent of fault orientation, has often proved effective (see King et al., 1994).

7. Conclusions

In this study, we conducted four experiments involving a sawcut red felser sandstone sample, each with a four-phase stressing history. The experiments varied in the rate of each loading phase and the influence of a displacement hold was explored.

We generally observed good agreement between the observed acoustic emissions (AE) and the basic Coulomb rate-and-state theory. Although theoretically, only one parameter, A, should need adjustment, we found that to accurately match the absolute number of events, it was also necessary to adjust r, which was between 1.5 and 2.2 times larger than what should theoretically be measurable from the initial loading cycle. This suggests a possible higher-order dependence of r on the instantaneous stressing rate, although it remains unclear whether this result is directly applicable to field observations, given the larger stress steps involved in our experiments compared to typical field-scale applications. The estimates of parameter A were broadly consistent with values from laboratory experiments, and three of the four experiments could be fitted with a single value of A.

Our stressing history tested various theoretical predictions, such as a constant rate of seismicity (here AE) at a constant stressing rate. It also examined the development of the Kaiser effects, the decay of seismicity at a hold, and if discontinued loading would result in a stress threshold (although this threshold was too small to resolve in our experiments). The theory was consistent with the observed AE production in all these scenarios.

We suggest that Coulomb rate-and-state models may be useful in various applications of AE monitoring, whether in simulations, experimental settings, structural health monitoring, and and for subsurface geothermal or CO2/H2 storage operations.

CRediT authorship contribution statement

Elías Rafn Heimisson: Writing – review & editing, Writing – original draft, Visualization, Software, Methodology, Investigation, Funding acquisition, Formal analysis, Data curation, Conceptualization. **Milad Naderloo:** Writing – review & editing, Methodology, Investigation, Data curation. **Debanjan Chandra:** Writing – review & editing, Methodology, Investigation. **Auke Barnhoorn:** Resources, Project administration, Funding acquisition, Conceptualization.

Declaration of competing interest

The authors declare that they have no known competing financial interests or personal relationships that could have appeared to influence the work reported in this paper.

Acknowledgements

This work benefited from EPOS-NL Facility Access to Delft Petrophysics Lab, DPL, TU Delft, supported by the Dutch Research Council (NWO). ERH thanks the Swiss National Science Foundation for partially supporting this research through the Ambizione grant number PZ00P2 208993. The data necessary to replicated the results of this work is available in Zenodo repository https://doi.org/10.5281/zenodo.12585821 (Heimisson et al., 2024). The authors acknowledge the technical support from Marc Friebel and Jens van den Berg to set up the deformation experiments. We acknowledge the constructive feedback provided by two anonymous reviewers.

Appendix A. Supplementary data

Supplementary data to this article can be found online at https://doi.org/10.1016/j.tecto.2024.230574.

Data availability

Data is available in a repository, link and reference in acknowledgements

References

Byerlee, J., 1978. Friction of Rocks. Birkhäuser Basel, Basel, pp. 615–626. https://doi.org/10.1007/978-3-0348-7182-2_4. ISBN 978-3-0348-7182-2.

Candela, T., Osinga, S., Ampuero, J.-P., Wassing, B., Pluymaekers, M., Fokker, P.A., van Wees, J.-D., de Waal, H.A., Muntendam-Bos, A.G., 2019. Depletion-induced seismicity at the Groningen gas field: Coulomb rate-and-state models including differential compaction effect. J. Geophys. Res. Solid Earth 124 (7), 7081–7104. https://doi.org/10.1029/2018JB016670.

Carpinteri, A., Lacidogna, G., Pugno, N., 2006. Richter's laws at the laboratory scale interpreted by acoustic emission. Mag. Concr. Res. 58 (9), 619–625. https://doi.org/10.1680/macr.2006.58.9.619.

Cattania, C., Hainzl, S., Wang, L., Enescu, B., Roth, F., 2015. Aftershock triggering by postseismic stresses: a study based on coulomb rate-and-state models. J. Geophys. Res. Solid Earth 120 (4), 2388–2407. https://doi.org/10.1002/2014JB011500.

Cebry, S.B.L., Ke, C.-Y., McLaskey, G.C., 2022. The role of background stress state in fluid-induced aseismic slip and dynamic rupture on a 3-m laboratory fault. J. Geophys. Res. Solid Earth 127 (8), e2022JB024371. https://doi.org/10.1029/2022JB024371. URL. https://agupubs.onlinelibrary.wiley.com/doi/abs/10.1029/2022JB024371.

Daley, D.J., Vere-Jones, D., et al., 2003. An Introduction to the Theory of Point Processes: Volume I: Elementary Theory and Methods. Springer.

Dieterich, J.H., 1972. Time-dependent friction in rocks. J. Geophys. Res. (1896-1977) 77 (20), 3690–3697. https://doi.org/10.1029/JB077i020p03690.

Dieterich, J.H., 1979. Modeling of rock friction: 1. Experimental results and constitutive equations. J. Geophys. Res. Solid Earth 84 (B5), 2161–2168. https://doi.org/10.1029/JB084iB05p02161.

Dieterich, J.H., 1981. Potential for geophysical experiments in large scale tests. Geophys. Res. Lett. 8 (7), 653–656. https://doi.org/10.1029/GL008i007p00653.

Dieterich, J., 1994. A constitutive law for rate of earthquake production and its application to earthquake clustering. J. Geophys. Res. Solid Earth 99 (B2), 2601–2618. https://doi.org/10.1029/93JB02581.

Green, R.G., Greenfield, T., White, R.S., 2015. Triggered earthquakes suppressed by an evolving stress shadow from a propagating dyke. Nat. Geosci. 8 (8), 629–632. https://doi.org/10.1038/ngeo2491.

Guglielmi, Y., Cappa, F., Avouac, J.-P., Henry, P., Elsworth, D., 2015. Seismicity triggered by fluid injection–induced aseismic slip. Science 348 (6240), 1224–1226. https://doi.org/10.1126/science.aab0476.

Guglielmi, Y., Nussbaum, C., Cappa, F., De Barros, L., Rutqvist, J., Birkholzer, J., 2021. Field-scale fault reactivation experiments by fluid injection highlight aseismic leakage in caprock analogs: Implications for CO2 sequestration. Int. J. Greenh. Gas Contr. 111, 103471. https://doi.org/10.1016/j.ijggc.2021.103471.

Hainzl, S., Steacy, S., Marsan, D., 2010. Seismicity Models Based on Coulomb Stress Calculations.

Harris, R.A., Simpson, R.W., 1998. Suppression of large earthquakes by stress shadows: a comparison of coulomb and rate-and-state failure. J. Geophys. Res. Solid Earth 103 (B10), 24439–24451. https://doi.org/10.1029/98JB00793.

Heimisson, E.R., 2019. Constitutive law for earthquake production based on rate-and-state friction: Theory and application of interacting sources. J. Geophys. Res. Solid Earth 124 (2), 1802–1821. https://doi.org/10.1029/2018JB016823.

Heimisson, E.R., Segall, P., 2018. Constitutive law for earthquake production based on rate-and-state friction: Dieterich 1994 revisited. J. Geophys. Res. Solid Earth 123 (5), 4141–4156. https://doi.org/10.1029/2018JB015656.

Heimisson, E.R., Segall, P., 2020. Physically consistent modeling of dike-induced deformation and seismicity: Application to the 2014 Bárðarbunga dike, Iceland. J. Geophys. Res. Solid Earth 125 (2), e2019JB018141. https://doi.org/10.1029/2019JB018141.

Heimisson, E.R., Einarsson, P., Sigmundsson, F., Brandsdóttir, B., 2015. Kilometer-scale Kaiser effect identified in Krafla volcano, Iceland. Geophys. Res. Lett. 42 (19), 7958–7965. https://doi.org/10.1002/2015GL065680.

Heimisson, E.R., Smith, J.D., Avouac, J.-P., Bourne, S.J., 2021. Coulomb threshold rate-and-state model for fault reactivation: application to induced seismicity at

Groningen. Geophys. J. Int. 228 (3), 2061–2072. https://doi.org/10.1093/gji/ggab467. ISSN 0956-540X.

Heimisson, E., Naderloo, M., Chandra, D., Barnhoorn, A., July 2024. Dataset Accompanying: "Applying and Validating Coulomb Rate-and-State Seismicity Models in Acoustic Emission experiments". https://doi.org/10.5281/zenodo.12585821.

Ke, C.-Y., McLaskey, G.C., Kammer, D.S., 2018. Rupture termination in laboratory-generated earthquakes. Geophys. Res. Lett. 45 (23), 12,784–12,792. https://doi.org/10.1029/2018GL080492.

Kilgore, B., Lozos, J., Beeler, N., Oglesby, D., 2012. Laboratory observations of fault strength in response to changes in normal stress. J. Appl. Mech. 79 (3), 031007. https://doi.org/10.1115/1.4005883.

King, G.C.P., Stein, R.S., Lin, J., 1994. Static stress changes and the triggering of earthquakes. Bull. Seismol. Soc. Am. 84 (3), 935–953. https://doi.org/10.1785/BSSA0840030935. ISSN 0037-1106.

Lavrov, A., 2003. The Kaiser effect in rocks: principles and stress estimation techniques. Int. J. Rock Mech. Min. Sci. 40 (2), 151–171. https://doi.org/10.1016/S1365-1609(02)00138-7. ISSN 1365-1609.

Lei, X., Ma, S., 2014. Laboratory acoustic emission study for earthquake generation process. Earthq. Sci. 27, 627–646. https://doi.org/10.1007/s11589-014-0103-y.

Linker, M.F., Dieterich, J.H., 1992. Effects of variable normal stress on rock friction: Observations and constitutive equations. J. Geophys. Res. Solid Earth 97 (B4), 4923–4940. https://doi.org/10.1029/92JB00017.

Lockner, D., 1993. The role of acoustic emission in the study of rock fracture. Int. J. Rock Mech. Min. Sci. Geomech. Abstr. 30 (7), 883–899. https://doi.org/10.1016/0148-9062(93)90041-B. ISSN 0148-9062.

Marone, C., 1998. Laboratory-derived friction laws and their application to seismic faulting. Annu. Rev. Earth Planet. Sci. 26, 643–696. ISSN 1545–4495. https://doi.org/10.1146/annurev.earth.26.1.643.

Naderloo, M., Ramesh Kumar, K., Hernandez, E., Hajibeygi, H., Barnhoorn, A., 2023a. Experimental and numerical investigation of sandstone deformation under cycling loading relevant for underground energy storage. J. Energy Storage 64, 107198. https://doi.org/10.1016/j.est.2023.107198.

Naderloo, M., Veltmeijer, A., Jansen, J., Barnhoorn, A., 2023b. Laboratory study on the effect of stress cycling pattern and rate on seismicity evolution. Geomech. Geophys. Geo-Energy Geo-Resour. 9 (1), 137. https://doi.org/10.1007/s40948-023-00678-1.

Norbeck, J.H., Rubinstein, J.L., 2018. Hydromechanical earthquake nucleation model forecasts onset, peak, and falling rates of induced seismicity in Oklahoma and Kansas. Geophys. Res. Lett. 45 (7), 2963–2975. https://doi.org/10.1002/2017GL076562.

Perfettini, H., Frank, W.B., Marsan, D., Bouchon, M., 2018. A model of aftershock migration driven by afterslip. Geophys. Res. Lett. 45 (5), 2283–2293. https://doi.org/10.1002/2017GL076287.

Prakash, V., 1998. Frictional response of sliding interfaces subjected to time varying normal pressures. J. Tribol. 120 (1), 97–102. https://doi.org/10.1115/1.2834197. ISSN 0742-4787.

Ruina, A., 1983. Slip instability and state variable friction laws. J. Geophys. Res. Solid Earth 88 (B12), 10359–10370. https://doi.org/10.1029/JB088iB12p10359.

Simpson, D., Leith, W., Scholz, C., 1988. Two types of reservoir-induced seismicity. Bull. Seismol. Soc. Am. 78 (6), 2025–2040. https://doi.org/10.1785/BSSA0780062025. ISSN 0037-1106.

Vilhelm, J., Rudajev, V., Ponomarev, A., Smirnov, V., Lokajícek, T., 2017. Statistical study of acoustic emissions generated during the controlled deformation of migmatite specimens. Int. J. Rock Mech. Min. Sci. 100, 83–89. https://doi.org/10.1016/j.ijrmms.2017.10.011. ISSN 1365-1609.

Zhai, G., Shirzaei, M., Manga, M., Chen, X., 2019. Pore-pressure diffusion, enhanced by poroelastic stresses, controls induced seismicity in Oklahoma. Proc. Natl. Acad. Sci. 116 (33), 16228–16233. https://doi.org/10.1073/pnas.1819225116.